



1 **Moment tensor catalogue of microearthquakes in West Bohemia from** 2 **2008 to 2018**

3
4 Václav Vavryčuk¹, Petra Adamová¹, Jana Doubravová¹, Josef Horálek¹

5
6 ¹Institute of Geophysics, Boční II/1401, 14100 Praha 4, Czech Republic

7
8 **Correspondence:** Václav Vavryčuk (vv@ig.cas.cz)

9 10 **Abstract**

11 We present a unique catalogue of full moment tensors (MTs) of microearthquakes that occurred in West
12 Bohemia, Czech Republic, in the period from 2008 to 2018. The catalogue is exceptional in several aspects:
13 (1) it represents an extraordinary extensive dataset of more than 5.000 MTs, (2) it covers a long period of
14 seismicity in the studied area, during which several prominent earthquake swarms took place, (3) the locations
15 and retrieved MTs of microearthquakes are of a high accuracy. Additionally, we provide three-component
16 records at the West Bohemia (WEBNET) seismic stations, the velocity model in the region, and the technical
17 specification of the stations. The dataset is ideal for being utilized by a large community of researchers for
18 various seismological purposes, e.g., for studies of (1) the migration of foci and the spatiotemporal evolution
19 of seismicity, (2) redistribution of stress during periods of intense seismicity, (3) the interaction of faults, (4)
20 the Coulomb stress along the faults and local stress anomalies connected to fault irregularities, (5) diffusivity
21 of fluids along the activated faults, or (6) the time-dependent seismic risk due to the migration of seismicity in
22 the region. In addition, the dataset is optimum for developing and testing new inversions for MTs and for
23 tectonic stress. Since most of the earthquakes are non-shear, the dataset can contribute to studies of non-double-
24 couple components of MTs and their relation to shear-tensile fracturing and/or seismic anisotropy in the focal
25 zone.

26 27 28 **1 Introduction**

29 The seismic moment tensor (MT) describes equivalent body forces acting at an earthquake source (Knopoff
30 and Randall, 1970). It is a basic quantity evaluated for earthquakes that informs us about their moment
31 magnitude, focal mechanism and type of faulting. It is formed by double-couple (DC), isotropic (ISO) and
32 compensated linear vector dipole (CLVD) components (Jost and Hermann, 1998; Vavryčuk, 2015). The DC
33 component is produced by shear faulting in isotropic media; the ISO and CLVD components reflect
34 complexities in the earthquake source, e.g., irregularly shaped faults, seismic anisotropy, shear-tensile faulting
35 induced by fluid injection in volcanic or geothermal areas, or the presence of a material interface in the focal



36 zone (Frohlich, 1994; Julian et al. 1998; Miller et al. 1998; Šílený and Milev, 2008; Vavryčuk 2005, 2006,
37 2011a, 2013, 2015; Vavryčuk and Hrubcová 2017).

38

39 Since earthquakes do not occur separately but in sequences, it is necessary to compile high-quality MT
40 catalogues for understanding origins of seismicity, tectonic stress regime and seismic energy release of any
41 region under study. In this way, we can identify prominent periods of seismicity, trace faults and fault
42 segments, monitor migration of earthquake foci, analyse interactions of nearby or intersecting faults, and map
43 the fluid flow along the fault systems in the focal zone (Vavryčuk et al., 2021). Hence, MT catalogues are
44 fundamental sources of information for all detailed studies of seismicity on the local, regional or global scale.

45

46 In this paper, we present recordings, locations and high-quality moment tensors of 5182 microearthquakes that
47 occurred in the West Bohemia geothermal region, Czech Republic in the period from 2008 to 2018. The
48 microearthquakes were monitored by the West Bohemia local seismic network WEBNET (Horálek et al.,
49 2000; Fischer et al., 2010). Their locations were calculated by the double-difference location method and the
50 moment tensors were determined using the moment tensor inversion of P waves based on the principal
51 component analysis. Because of its extent and quality, the presented dataset is unique and represents an
52 extraordinary dataset, which might find exciting applications in numerous future studies.

53

54 **2 West-Bohemia seismoactive region**

55 The region of West Bohemia is located in the western part of the Bohemian Massif, where three major tectonic
56 units are merged: the Saxothuringian, the Teplá-Barrandian and the Moldanubian. The region is
57 geodynamically active exposed to the Tertiary and Quaternary volcanism associated with CO₂ emanations,
58 dry and wet mofettes, and numerous mineral springs (Kämpf et al., 2013; Hrubcová et al., 2017; Bräuer et al.,
59 2018). Two major fault systems are identified in the area: the Mariánské Lázně fault striking in the NW-SE
60 direction and the Ore-Mountain fault striking in the WSW-ENE direction (Figure 1b). The recently most active
61 fault is, however, a left-lateral strike-slip fault in the N-S direction, situated at the eastern boundary of the Cheb
62 Basin filled by up to 300 m thick Tertiary and Quaternary sediments. The seismically active faults were
63 identified at depth by clustering of hypocentres and by focal mechanisms (Vavryčuk et al., 2013), but they also
64 have some geological evidence on the surface (Bankwitz et al., 2003).

65

66 The seismic energy in the West Bohemia region is typically released in the form of earthquake swarms. The
67 occurrence of the earthquake swarms has been well documented in the region since the beginning of the 19th
68 century. A significant increase of the earthquake activity was observed at the turn of the 19th and 20th century,
69 when several larger swarms were observed. There were earthquake swarms in 1897, 1900, 1903 and 1908.
70 During the last 40 years, the seismicity occurs in the area of 40 x 50 square kilometres, but the most intense
71 seismicity is focused in the Nový Kostel zone with size of 3 x 12 square kilometres (Fischer et al., 2014;
72 Čermáková and Horálek, 2015). Foci of microearthquakes in this zone are clustered along a fault striking in
73 the roughly N-S direction (Figure 1a) with depths ranging from 6 to 11 km. The duration of the earthquake



74 swarms varies; it lasts from several days for micro-swarms up to 2-3 months for the most prominent swarms.
75 The swarms may consist of several thousands of microearthquakes. The local magnitudes M_L of the
76 microearthquakes rarely exceed a value of 4.0. The strongest instrumentally recorded swarm activity occurred
77 in 1985/86 with two main shocks having magnitudes of M_L 4.6 and 4.2.

78
79
80
81
82
83
84
85
86
87
88
89
90
91
92
93
94
95
96
97
98
99
100
101
102
103
104
105
106
107
108
109
110
111
112
113
114
115
116
117
118
119
120
121

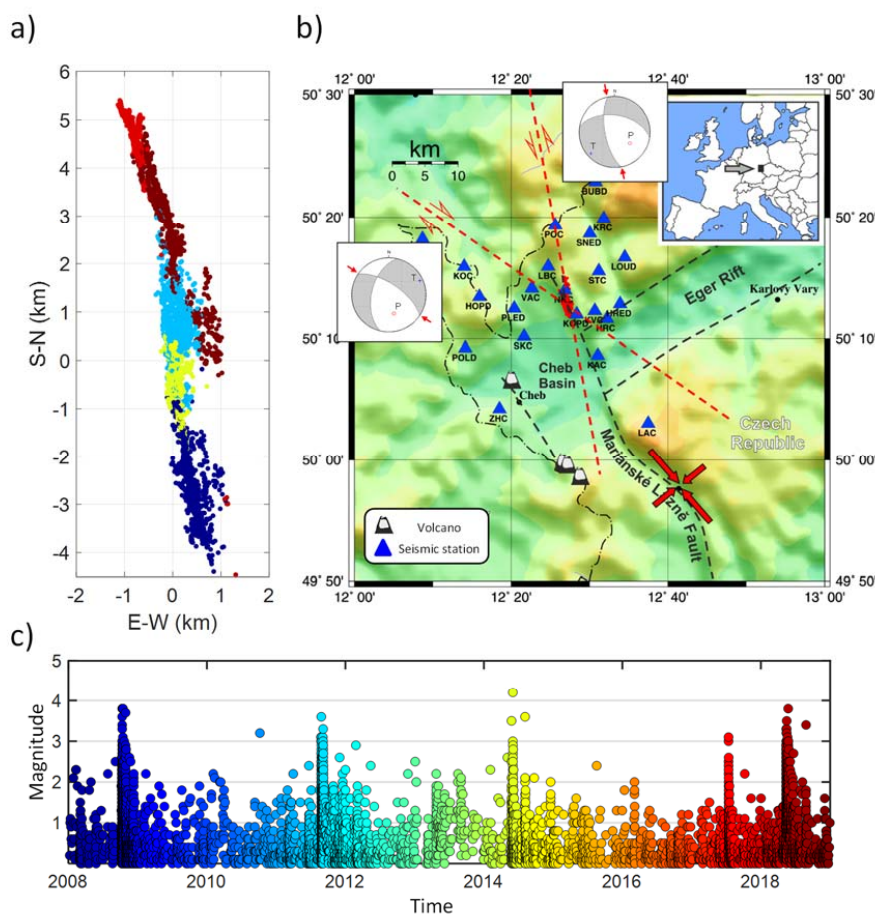


Figure 1. (a) The map view of earthquake foci in the period from 2008 to 2018, (b) topographic map with tectonic faults (black dashed lines) and positions of stations (blue triangles), and (c) the magnitude-time plot with the colour-coded time. The red dots in (b) show the earthquake foci. The red full arrows mark the orientation of the maximum and minimum principal stress axes. The dashed-dotted line marks the boundary between the Czech Republic and Germany. The position of West Bohemia in Europe is indicated in the inset. The focal mechanisms typical for the area are also indicated.



122 **3 Monitoring system**

123

124 The seismic activity in the region is monitored by the local seismic network WEBNET (Figure 1b, Table 1).
 125 The network was operating since 1994 and the number of stations gradually increased (Horálek et al., 2000;
 126 Fischer et al., 2010). After its major upgrade in 2008, the WEBNET network consists of 23 seismic stations
 127 within the epicentral distance of 25 km. The stations cover the area uniformly with no azimuthal gaps. The
 128 three component ground-velocity records are sampled at 250 Hz and the frequency response is flat at least
 129 between 1 and 80 Hz. Until September 2014, all data were processed based on triggered records. Since the
 130 beginning of September 2014, the recordings are processed by using automatic pre-processing of continuous
 131 recordings. Another major upgrade of the network was realized in 2015. Originally, the stations were equipped
 132 by the Le-3DLite and SM3 seismometers; some of them were lately upgraded using the Guralp CMG-3ESP
 133 seismometers. The station with the nearest epicentral distance (station NKC) is additionally equipped with the
 134 broadband STS-2 seismometer. For a detailed technical specification of the WEBNET seismic stations, see
 135 Table 1.

136

137 **Table 1.** Location and instrumentation of the WEBNET seismic stations

138

Code	Site name	Latitude (°N)	Longitude (°E)	<i>h</i> (m)	Sensor before 2015	Digitizer before 2015	Sensor after 2015	Digitizer after 2015	Note
BUBD	Bublava	50.38174	12.51362	746	LE-3DLite	Gaia	LE-3DLite	Gaia	
HOPD	Horní Paseky	50.22378	12.26547	731	LE-3DLite	Gaia	LE-3DLite	Gaia	
HRC	Hrádek	50.19348	12.53660	596	LE-3DLite	Gaia	LE-3DLite	Gaia	Out of order from 2015
HRED	Hřebeň	50.21425	12.56491	589	LE-3DLite	Gaia	LE-3DLite	Gaia	
HUC	Komorní Hůrka	50.09997	12.33612	480	-	-	CMG-3ESPC	Taurus	Installed in 2016
KAC	Kaceřov	50.14361	12.51708	548	SM-3	Janus-Trident	SM-3	Janus-Trident	
KOC	Kopaniny	50.26417	12.23288	621	SM-3	5800 PCM	CMG-3ESPC	Centaur	
KOPD	Kopanina	50.20319	12.47473	536	LE-3DLite	Gaia	LE-3DLite	Gaia	
KRC	Kraslice	50.33069	12.52950	806	SM-3	Janus-Trident	CMG-3ESPC	Centaur	
KVC	Květná	50.20496	12.51134	666	SM-3	5800 PCM	CMG-3ESPC	Centaur	



LAC	Lazy	50.04967	12.62396	884	SM-3	5800 PCM	CMG- 3ESPC	Centaur	
LBC	Luby	50.26461	12.41123	684	SM-3	Janus- Trident	CMG- 3ESPC	Centaur	
LOUD	Loučná	50.27753	12.57449	692	LE-3DLite	Gaia	LE- 3DLite	Gaia	
NKC	Nový Kostel	50.23234	12.44706	610	SM-3 CMG-40T	5800 PCM Janus- Trident	CMG- 3ESPC STS-2	Centaur	
PLED	Plesná	50.20890	12.33767	556	LE-3DLite	Gaia	LE- 3DLite	Gaia	
POC	Počátky	50.31997	12.42662	841	SM-3	Janus- Trident	CMG- 3ESPC	Centaur	
POLD	Polná	50.15603	12.23497	556	LE-3DLite	Gaia	LE- 3DLite	Gaia	
SKC	Skalná	50.16911	12.36050	501	SM-3	Janus- Trident	CMG- 3ESPC	Centaur	
SNED	Sněžná	50.31088	12.50131	756	LE-3DLite	Gaia	LE- 3DLite	Gaia	
STC	Studenec	50.25794	12.51849	712	SM-3	Janus- Trident	CMG- 3ESPC	Centaur	
TRC	Trojmezí	50.30344	12.14466	612	LE-3DLite	Gaia	CMG- 3ESPC	Centaur	
VAC	Vackov	50.23450	12.37634	581	SM-3	Janus- Trident	CMG- 3ESPC	Centaur	
ZHC	Zelená Hora	50.06984	12.30810	677	CMG-40T	Janus- Trident	CMG- 3ESPC	Centaur	
MAC	Chlum sv. Maří	50.14429	12.53516	609	-	-	CMG- 3ESPC	Centaur	Installed in 2017

139 Quantity h means the altitude of the stations. Recording systems: Taurus – Nanometrics digitizer; Janus-Trident
 140 – Nanometrics communications controller-digitizer; Centaur – Nanometrics digitizer; Gaia – Vistec digitizer;
 141 5800 PCM – Lennartz digitizing system. Seismometers: SM-3 – SP sensor; LE-3DLite – Lennartz SP sensor;
 142 CMG-40T – Guralp BB sensor; CMG-3ESPC – Guralp BB sensor.

143

144

145 4 Seismicity in 2008-2018

146 The West Bohemia region is characterized by a continuous background seismicity scattered over the whole
 147 region interrupted by earthquake swarm sequences located mostly in the Nový Kostel focal zone. The most
 148 intense periods of seismicity in 2008, 2011, 2014, 2017 and 2018 (Figures 1c and 2). All these sequences are
 149 typical earthquake swarms except for the seismic activity in 2014, which was exceptional. This sequence
 150 resembled a mainshock-aftershock sequence rather than the earthquake swarm (Hainzl et al., 2016; Jakoubková
 151 et al., 2018; Vavryčuk and Adamová, 2018) being formed by three pronounced activity periods. The strongest



152 events in these periods reached magnitude significantly larger than the other events (Figure 2c). The seismic
153 sequences differ in the earthquake productivity, in the duration, and in the number of periods of the intense
154 seismicity (Figure 2). The strongest event in the period from 2008 to 2018 reached magnitude M_L of 4.2 and
155 it occurred in 2014.

156

157

158

159

160

161

162

163

164

165

166

167

168

169

170

171

172

173

174

175

176

177

178

179

180

181

182

183

184

185

186

187

188

189

190

191

192

193

194

195

196

197

198

199

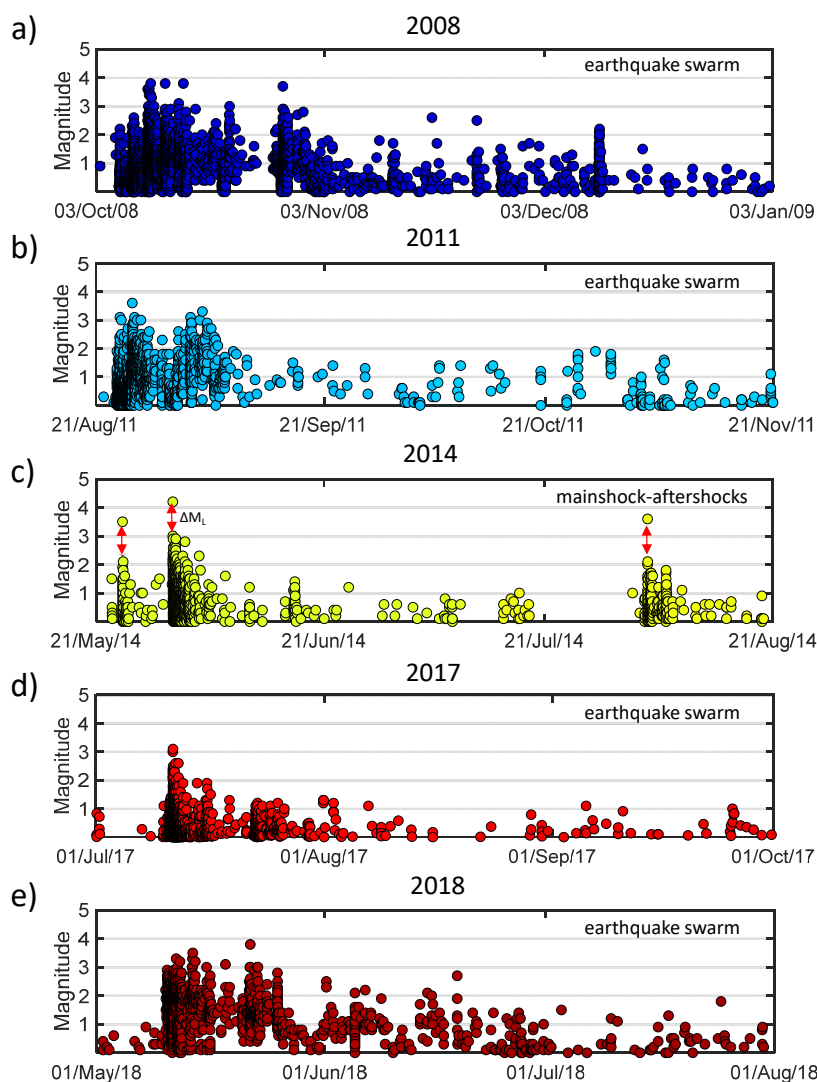


Figure 2. Magnitude-time plots of the major seismic sequences in the period from 2008 to 2018. According to the Bath law (Bath, 1965), the 2014 activity resembles rather a mainshock-aftershock sequence, because the difference in magnitudes ΔM_L between two strongest events in individual seismicity phases exceeds 1. In other seismic sequences, the magnitude gaps between two strongest events are not so prominent.



200 **5 Magnitudes and foci locations**

201 The local magnitude of earthquakes is computed from the velocity records according to the formula of Horálek
202 et al. (2000). The locations are computed in two steps. First, initial locations were calculated by the NonLinLoc
203 code (Lomax et al., 2009) in a layered velocity model (see Table 2) developed by Málek et al. (2005). For the
204 locations, manual picks of the P and S arrivals were used. Second, we applied the double-difference location
205 algorithm developed by Waldhauser and Ellsworth (2000) to differential times calculated from manual picks.
206 The relative precision of hypocentres was less than ± 20 m within the cluster (Bouchaala et al., 2013). The
207 absolute location of the cluster was determined with the accuracy of about ± 100 m in the horizontal plane and
208 ± 350 m in depth (see Bouchaala et al., 2013).

209

210 The locations of foci point to complex geometry of the fault system in the focal area (Figure 3). The seismicity
211 migrated from south to north in time and the individual seismic sequences occurred along different subfaults
212 (Fischer et al., 2010; Bouchaala et al., 2013; Vavryčuk et al., 2013; Jakoubková et al., 2017). For example, the
213 2008, 2011 and 2017 swarms activated three similarly oriented subfaults separated with gaps and offsets
214 between them. The barrier between the fault segments activated in 2008 and 2011 was broken in 2014 (Hainzl
215 et al., 2016; Vavryčuk and Adamová, 2018), and the gap between the fault segments activated in 2011 and
216 2017 was broken during the 2018 swarm (Bachura et al., 2021; Vavryčuk et al., 2021). The overall direction
217 of the whole fault system is defined by strike of 170° and dip of 75° . However, some fault segments may
218 deviate from this overall direction significantly. For example, small echelon faults located at the deepest part
219 of the fault system have strike of 305° and dip of 65° (see Figure 3c, blue dots at the depth range of 10.5-11
220 km).

221

222

223

Table 2. The layered velocity model

Depth (km)	0.0	0.2	0.5	1.0	2.0	4.0	6.0	10.0	20.0	32.0
v_P (km/s)	4.30	5.06	5.33	5.60	5.87	6.09	6.35	6.74	7.05	7.25
Q_P	30	40	50	60	80	100	150	200	300	400

224

225 Ratio v_P/v_S is 1.70 and ratio Q_P/Q_S is 2.

226

227

228

229

230

231

232

233

234

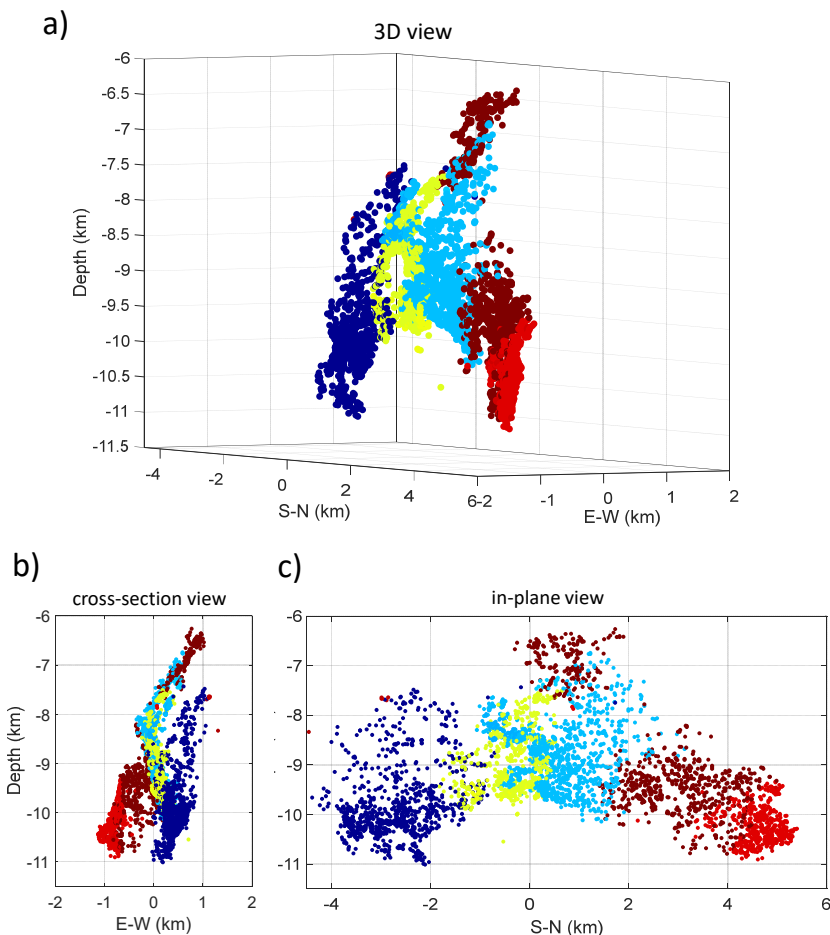
235

236

237



238
239
240
241
242
243
244
245
246
247
248
249
250
251
252
253
254
255
256
257
258
259
260
261
262
263
264
265
266
267
268
269
270
271
272
273



274 **Figure 3.** The earthquakes foci with local magnitude $M_L \geq 0.5$ in (a) 3D view, (b) cross-section vertical view,
275 and (c) in-plane vertical view. The foci are colour coded according to time: dark blue – 2008, light blue – 2011,
276 yellow – 2014, red – 2017, and brown – 2008.

277
278
279

6 Moment tensors

280
281

6.1 MT inversion of microearthquakes

282 The MT inversion requires accurate locations of earthquakes, an accurate crustal velocity model, dense
283 coverage of stations on the focal sphere and low seismic noise (Šílený, 2009; Ford et al., 2010; Stierle,
284 Bohnhoff, et al., 2014; Stierle, Vavryčuk, et al., 2014). We can invert amplitudes of seismic phases, amplitude
285 ratios or full waveforms (Dreger and Woods, 2002; Cesca et al., 2006; Sokos and Zahradník, 2008; Cesca and
286 Dahm, 2008; Vavryčuk et al., 2008; Zahradník et al., 2008; Fojtíková et al., 2010; Kwiątek et al., 2016;



287 Jechumtálová and Šílený, 2005; Vavryčuk and Kühn, 2012; Yu et al., 2018, 2019). Each inversion is applicable
288 to earthquake of different magnitudes, wave frequencies and epicentral distances of stations. MTs of moderate
289 or large earthquakes are usually calculated from full waveforms recorded at regional or global seismic
290 networks. By contrast, MTs of small earthquakes and microearthquakes are commonly calculated from
291 amplitudes of P and/or S waves picked in short-period seismograms recorded at local networks.

292

293 The inversion for MTs of microearthquakes is challenging for several reasons: (1) the waveforms are complex
294 due to high frequencies and noise, and (2) the datasets are extensive with thousands of events, which require a
295 semi- or fully-automated processing. Here, the MT inversion developed by Vavryčuk et al. (2017) is applied.
296 The inversion is based on the principal component analysis (PCA), which transforms correlated waveforms
297 into a set of the called principal components (see Figure 4). The first component has the highest variance and
298 reproduces a so-called ‘common wavelet’, i.e., a wavelet with the highest similarity with all analysed traces.
299 This common wavelet physically represents a signal radiated by the earthquakes source, which can be distorted
300 during its propagation from the source to the receiver by inhomogeneities in the geological structure, site
301 effects or seismic noise.

302

303 Subsequently, the common wavelet is correlated with individual recorded traces and the effective P-wave
304 amplitudes are calculated as the amplification factors applied to the common wavelet, in order to optimally
305 reproduce the recorded traces. The obtained amplitudes are inverted for the MTs using the generalized linear
306 inversion (Lay and Wallace, 1995). The Green’s function amplitudes are computed by the ray method
307 (Červený, 2001) and incorporated the effects of the Earth’s surface. An inhomogeneous medium with a vertical
308 gradient obtained by smoothing the layered model of Málek et al. (2005) was applied for computing the rays
309 by the ray-tracing algorithm. The inversion is robust, fast and insensitive to noise in data.

310

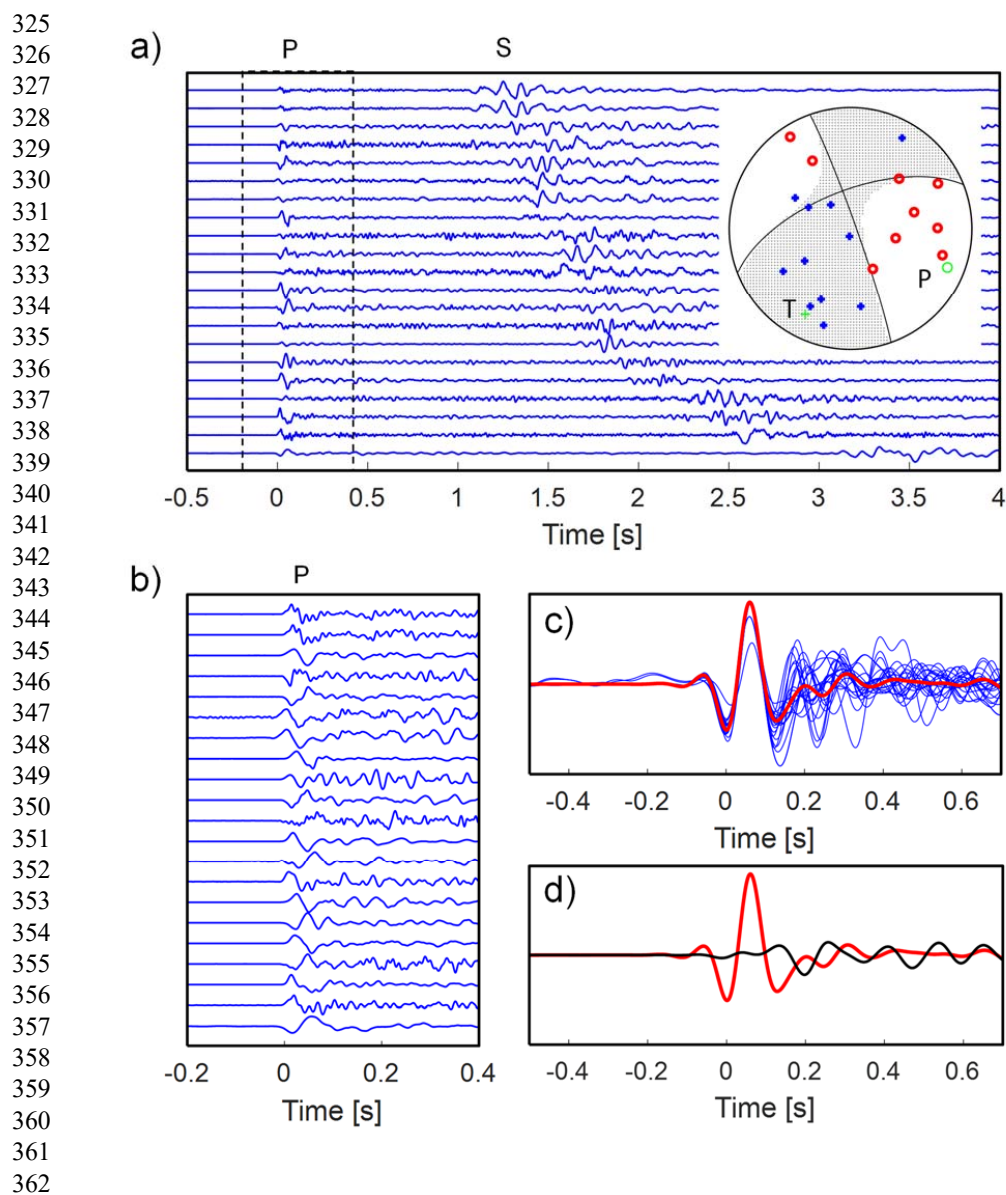
311

312 **6.2 Individual steps of the MT inversion**

313 The MT inversion consists of data pre-processing, alignment of traces, computation of the effective amplitudes
314 using the PCA method and the MT inversion. The individual steps of the inversion are as follows (see Figure
315 5):

316 1. Data pre-processing, which comprises: (a) an oversampling of records in order to perform an accurate
317 alignment of waveforms, (b) band-pass filtering to enhance the signal-to-noise ratio, and (c) a rough
318 alignment of waveforms using manual picks, if available, or using an automatic picking algorithm called
319 the Suspension Bridge Picking (SBPx), see FeedMeImATroll (2021).

320 2. Two-step accurate alignment of waveforms, which comprises: (a) an alignment of waveforms using the
321 cross-correlation with the waveform of the highest signal-to-noise ratio, (b) calculation of the first principal
322 component from the aligned waveforms, (c) another alignment of waveforms using the cross-correlation
323 with the computed first principal component, and (d) calculation of the refined first principal component
324 from the aligned waveforms.



363 **Figure 4.** Example of the MT inversion of the microearthquake on 24 May 2014 at 16:14:30 with ML 2.1. (a)
364 Whole velocity records; (b) window with aligned P waves; (c) the common wavelet (red line) together with
365 the P-wave traces at individual stations (blue lines); (d) the common wavelet represented by the first principal
366 component (red line) and noise in waveforms represented by the second principal component (black line). The
367 polarities of the P-wave in panel (c) are switched to be consistent with the polarity of the common wavelet.
368 The inset in plot (a) shows the focal mechanism and positions of stations on the focal sphere (red circles mark
369 negative polarities, and blue plus signs mark the positive polarities).

370
371



372 3. Calculation of the PCA amplitudes and weights in the MT inversion, which comprises: (a) calculation
 373 of the PCA coefficients of the first principal component, which serve as the effective amplitudes used in
 374 the MT inversion, (b) calculation of the correlation coefficients between individual traces and the first
 375 principal component, which serve as the weights in the linear MT inversion scheme (in this way, a station
 376 with a waveform significantly different from the common wavelet suppressed in the inversion),

377 4. Repeated MT inversion for several alternative band-pass filters and time windows, in order to adapt the
 378 inversion to earthquakes with a varying frequency content. The inversion is firstly run with the whole set
 379 of stations, and secondly with eliminating two stations producing the largest misfits in the inversion.

380 In this way, we obtain a set of candidate MTs. The optimum MT is that with the minimum root-mean-squares
 381 (RMS) of differences between the synthetic amplitudes A^{synth} and the observed amplitudes A^{obs}

382
$$RMS = \frac{\sqrt{\sum_{i=1}^N (A_i^{synth} - A_i^{obs})^2}}{\sqrt{\sum_{i=1}^N (A_i^{synth})^2}}, \quad (1)$$

383 where N is the number of stations. The optimum MT is normalized and expressed in a relative scale, because
 384 it is computed from wave amplitudes but not from full displacement records. The scalar moment is obtained
 385 by integrating the common (displacement) wavelet. The optimum MTs were further decomposed into the DC,
 386 ISO and CLVD components according to Equations (6-10) of Vavryčuk (2015).

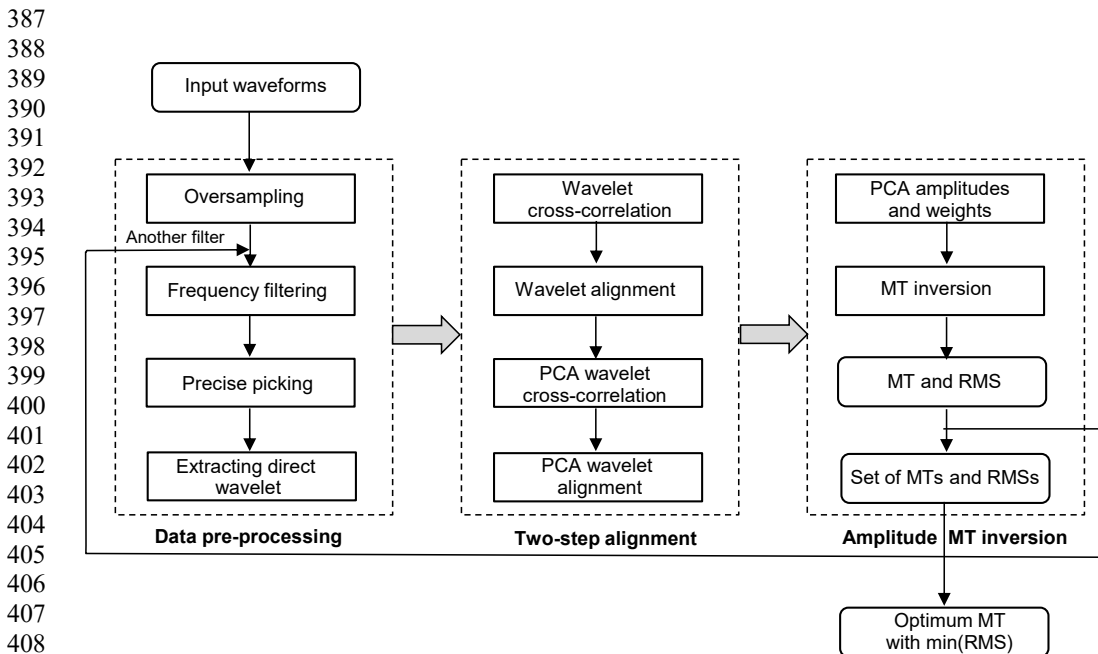


Figure 5. Flowchart of the PCA moment tensor inversion.



412
413
414
415
416
417
418
419
420
421
422
423
424
425
426
427
428
429
430
431
432
433
434
435
436
437
438
439
440
441
442
443
444
445
446
447
448
449
450
451
452
453
454
455
456
457
458
459
460
461
462
463
464
465

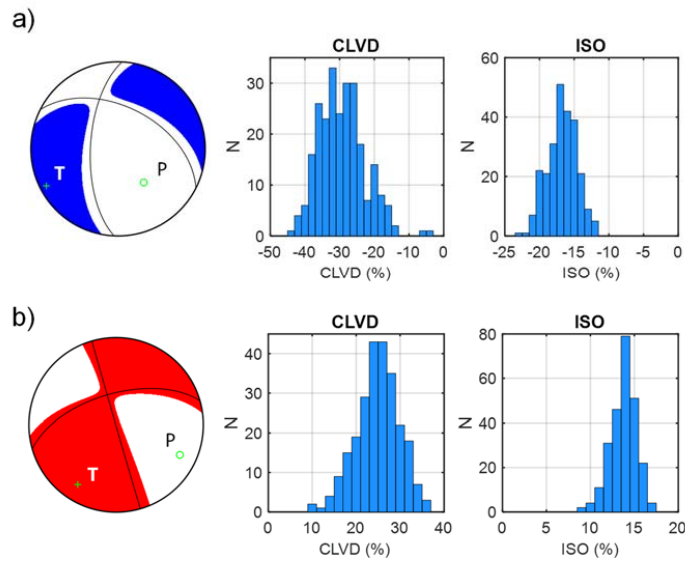


Figure 6. Examples of focal mechanisms and histograms of the CLVD and ISO errors. (a) Microearthquake on 1 September, 2011 at 12:54:05.7 with $ML = 0.6$, and (b) microearthquake on 11 May, 2018 at 06:26:09.0 with $ML = 2.3$.

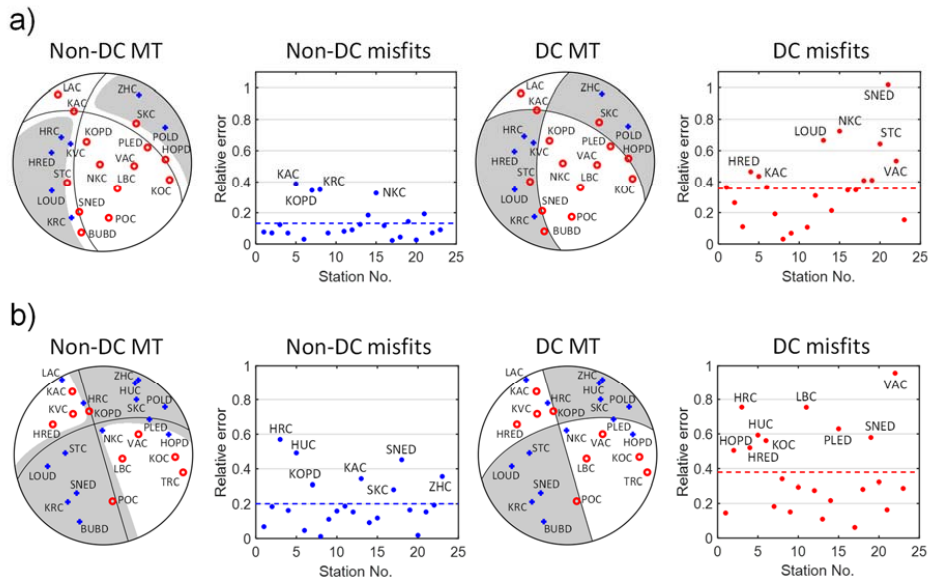


Figure 7. Inversion for the full MT solution (‘Non-DC MT’ and ‘Non-DC misfits’) and for the DC solution (‘DC MT’ and ‘DC misfits’) for microearthquakes in Figure 6. The mean amplitude misfits for the full MT and DC solutions are shown by blue and red dashed lines, respectively.



466 In order to estimate errors of the MTs, the inversion is performed for each MT repeatedly 100 times using
467 amplitudes distorted by noise characterized by a flat probability distribution. The level of noise ranges from -
468 25% to 25 % of the inverted amplitude at each trace. The scatter of the solutions served for estimating: (1) the
469 mean errors in the P/T axes directions calculated as the mean of deviations between the directions of the P/T
470 axes of noise-free solution and the noisy solutions, (2) the mean errors in the percentages of the DC, ISO and
471 CLVD components calculated as the standard deviations of the DC, ISO and CLVD values of noisy MT
472 solutions.

473
474 Figure 6 exemplifies the MT inversion for two micro-earthquakes, which display significant non-DC
475 components. The histograms of the CLVD and ISO errors indicate that the ISO component is always better
476 constrained than the CLVD component. Nevertheless, despite the numerical errors produced by the inversion,
477 the histograms prove that both the events contain also true non-DC components. This is also confirmed by a
478 comparison of fits for the full MTs and for the DC solutions for the events shown in Figure 7. The figure
479 indicates that the misfits for the full MT solutions are almost twice lower than those for the DC solutions. This
480 proves that at least some part of the non-DC components retrieved by the MT inversion should be of physical
481 origin.

482
483

484 7 Basic characteristics of the MT catalogue

485 Firstly, we processed all events with the local magnitude larger than 0.5. After that, we checked manually the
486 quality of input data and the retrieved MT and we excluded earthquakes: (1) recorded at a low number of
487 stations ($N < 14$), (2) with extremely low signal-to-noise ratio, (3) produced unstable moment tensors with
488 anomalously high RMS ($RMS > 1$). In this way, we obtained a dataset of 5182 earthquakes listed in the
489 catalogue. Table 3 summarizes the numbers of events in individual years. The magnitude-frequency
490 distribution of the analysed events is shown in Figure 8.

491
492
493
494

Table 3. Number of reported events for each year.

Year	2008	2009	2010	2011	2012	2013
Number of events	991	40	29	1225	69	201
Year	2014	2015	2016	2017	2018	2008-2018
Number of events	841	40	33	583	1130	5182

495
496
497
498
499



500
501
502
503
504
505
506
507
508
509
510
511
512
513
514
515
516
517
518
519
520
521
522
523
524
525
526
527
528
529
530
531
532
533
534
535
536
537
538
539
540
541
542
543
544
545

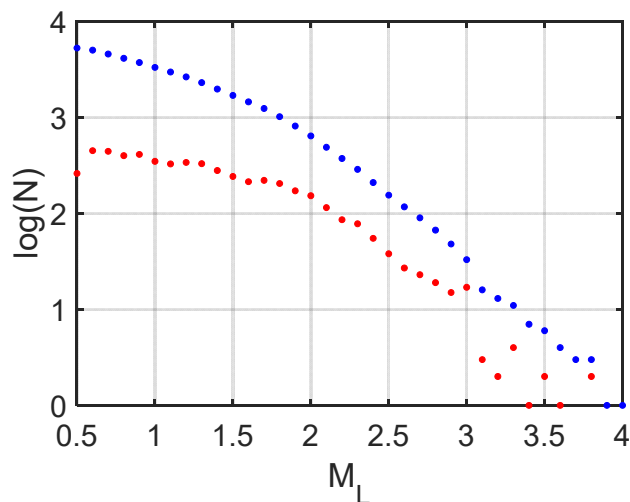
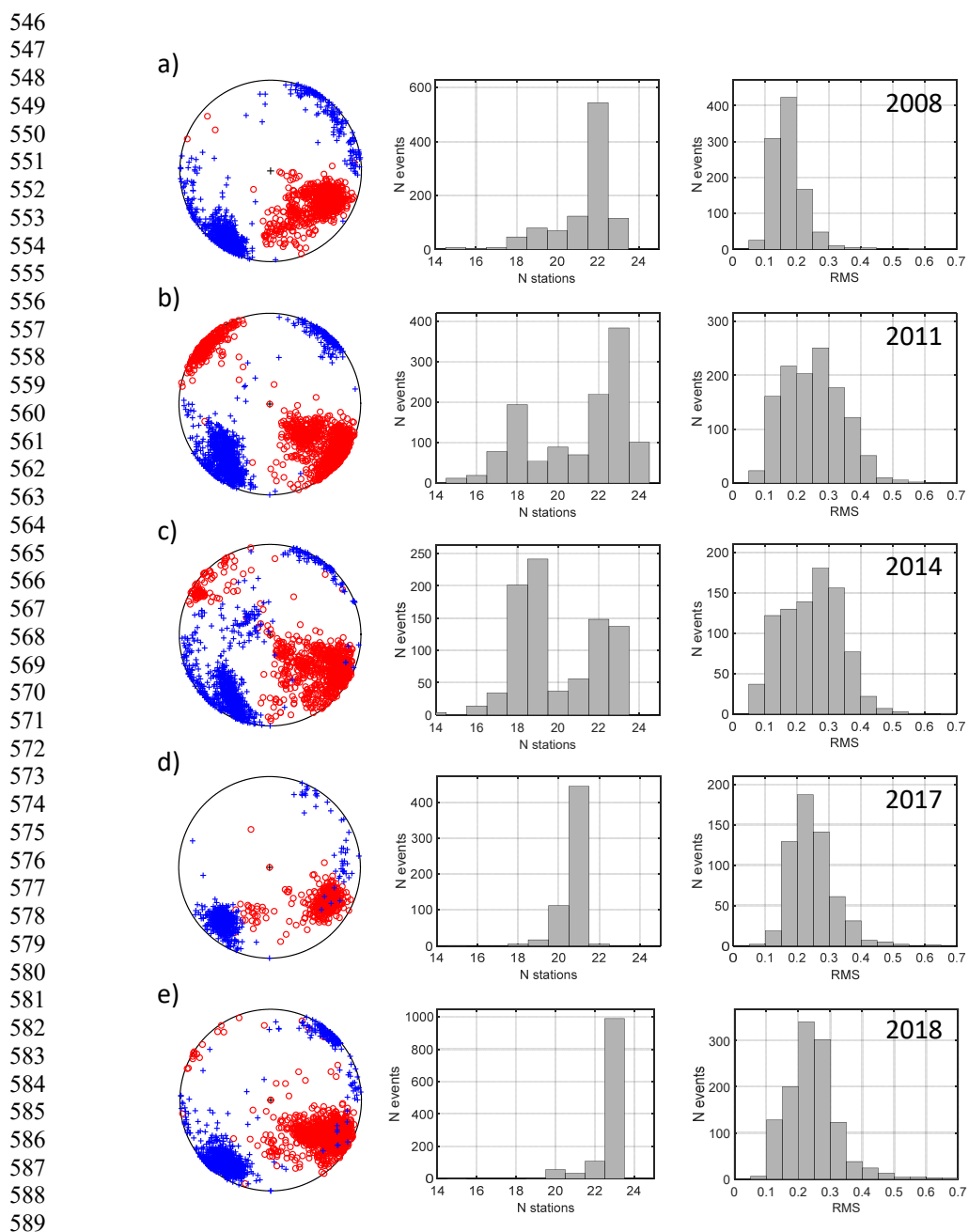


Figure 8. Cumulative (blue) and non-cumulative (red) magnitude-frequency distribution of the analysed earthquakes.

The earthquakes inverted for MTs were recorded mostly by 20 or more stations (Figure 9, middle column). The RMS varied during the whole period and ranged mostly from 0 to 0.5 (Figure 9, right column). The MTs with RMS higher than 0.5 were considered as unreliable. The variation of the RMS in time is probably produced by varying station coverage due to the foci migration. The P/T axes form compact and non-overlapping clusters for all seismic sequences in the studied time period (Figure 9). The position of clusters slightly differs in individual years and indicates some stress variation in the focal zone. Directions of the P/T axes are well resolved with the mean standard deviation less than 2° (Figure 10, two left columns). The errors of the ISO and CLVD components are mostly about 1.5-2% and 5-6%, respectively (Figure 10, two right columns). Comparing these errors for individual activity periods, we see that the errors tend to slightly decrease with time. This might be due to a continuously increasing quality of the WEBNET network. The histograms of the standard deviations of the P/T axes and the ISO and CLVD errors for the whole period from 2008-2018 are shown in Figure 11.



591 **Figure 9.** The P/T axes (left-hand plots), histograms of the RMS of the number of stations used in the MT
592 inversion (middle plots), and histograms of the RMS of the retrieved MTs (right-hand plots) for seismic
593 activities in 2008 (a), 2011(b), 2014 (c), 2017 (d) and 2018 (e). N denotes the number of stations, which
594 recorded the individual earthquakes.

595



596

597

598

599

600

601

602

603

604

605

606

607

608

609

610

611

612

613

614

615

616

617

618

619

620

621

622

623

624

625

626

627

628

629

630

631

632

633

634

635

636

637

638

639

640

641

642

643

644

645

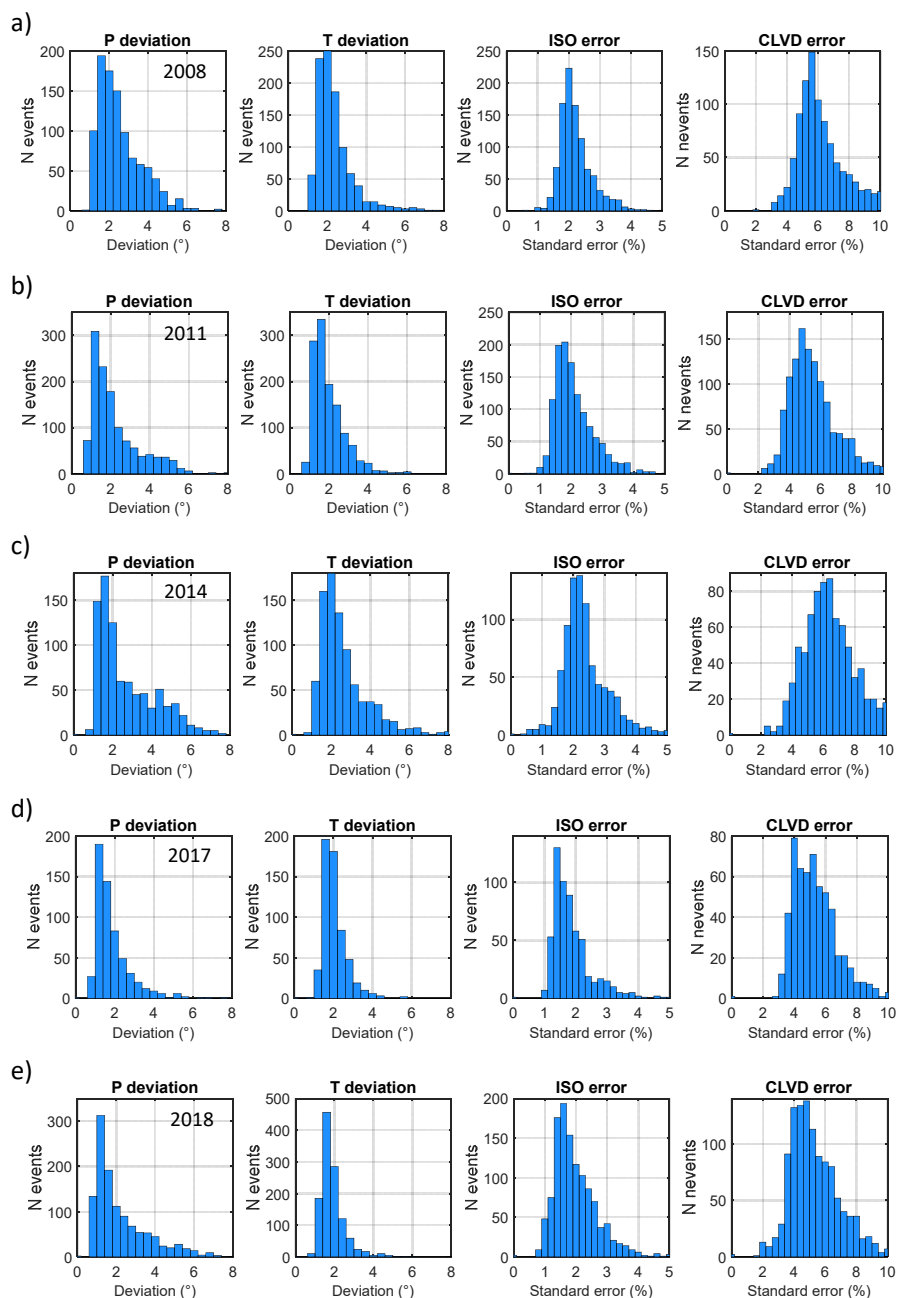


Figure 10. Histograms of mean deviations of the P/T axes and histograms of the ISO and CLVD standard errors for MTs of earthquakes from individual prominent seismic activities: in 2008 (a), 2011(b), 2014 (c), 2017 (d) and 2018 (e). The mean P/T deviations and the ISO and CLVD standard errors were calculated for each event from 100 MTs inverted using randomly generated noisy data.



646
647
648
649
650
651
652
653
654
655
656
657
658
659
660
661
662
663
664
665
666
667
668
669
670
671
672
673
674
675
676
677
678
679
680
681
682
683
684
685
686
687
688
689

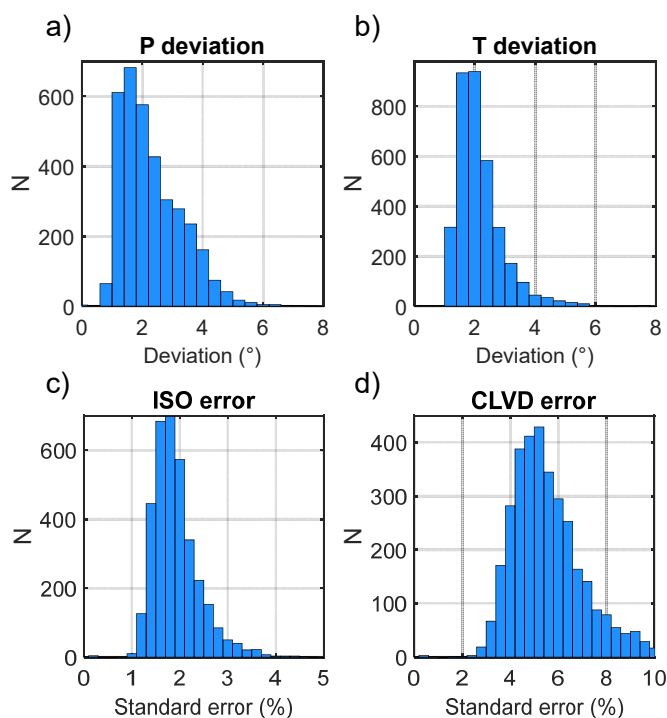


Figure 11. Histograms of mean deviations of the P/T axes (a-b) and histograms of the standard ISO and CLVD errors (c-d) for the 5182 reported MTs. The mean P/T deviations and the ISO and CLVD standard errors were calculated for each event from 100 MTs inverted using randomly generated noisy data.

8 Description of the dataset

The dataset consists of the following directories:

- Waveforms – this directory is further structured into subdirectories according to individual years and earthquakes. Three-component velocity records are stored in ASCII files with four columns (time + 3 components) individually for each station and each earthquake.
- Model – this directory contains the ASCII file ‘model.crust’, which defines the layered velocity model for the West Bohemia region (depth, P-wave velocity, v_P/v_S ratio, Q_P and Q_P/Q_S ratio).
- Stations – this directory contains the ASCII file ‘stations_Webnet.dat’ with coordinates of stations (site, name of the station, latitude, longitude, elevation).
- Moments – this directory contains the ASCII file ‘catalogue_2008-2018.dat’ with double difference locations, magnitudes, moment tensors and their errors, RMS and the numbers of inverted stations.
- Figures – this directory is further structures into subdirectories according to individual years. Four figures are provided for each earthquake (see Figure 12): complete waveforms of vertical components,



690 a detail of the P-waveforms, the focal mechanism with positions of stations, and the RMS at individual
691 stations.

692

693 File 'catalogue_2008-2018.dat' lists the following quantities for each earthquake:

- 694 • Event identification (composed form year and the sequential number of the event in the year)
- 695 • Double-difference locations
- 696 • Origin time (year, day, hour, minute, second)
- 697 • Latitude (°N)
- 698 • Longitude (°E)
- 699 • Depth (km)
- 700 • Local magnitude M_L (calculated according to Horálek et al., 2000)
- 701 • N – number of stations used in the MT inversion
- 702 • Frequencies f_1 a f_2 (in Hz) – optimum parameters of the Butterworth band-pass filter
- 703 • RMS – for its definition, see Equation (1)
- 704 • Moment magnitude M_w
- 705 • Components of the normalized moment tensor: M_{11} , M_{12} , M_{13} , M_{22} , M_{23} , M_{33} (x_1 – North, x_2 – East, x_3
706 – down). The moment tensor is normalized using the Euclidean norm (see Equation 17 of Vavryčuk,
707 2015)
- 708 • Strike1, dip1, rake1, strike2, dip2, rake2 (in °)
- 709 • DC, CLVD, ISO (in %, calculated according to Equations 6-10 of Vavryčuk, 2015)
- 710 • Errors of DC, CLVD, ISO (in %, for the definition of errors, see the text)
- 711 • Deviations of the P/T axes (in °, for the definition of errors, see the text)

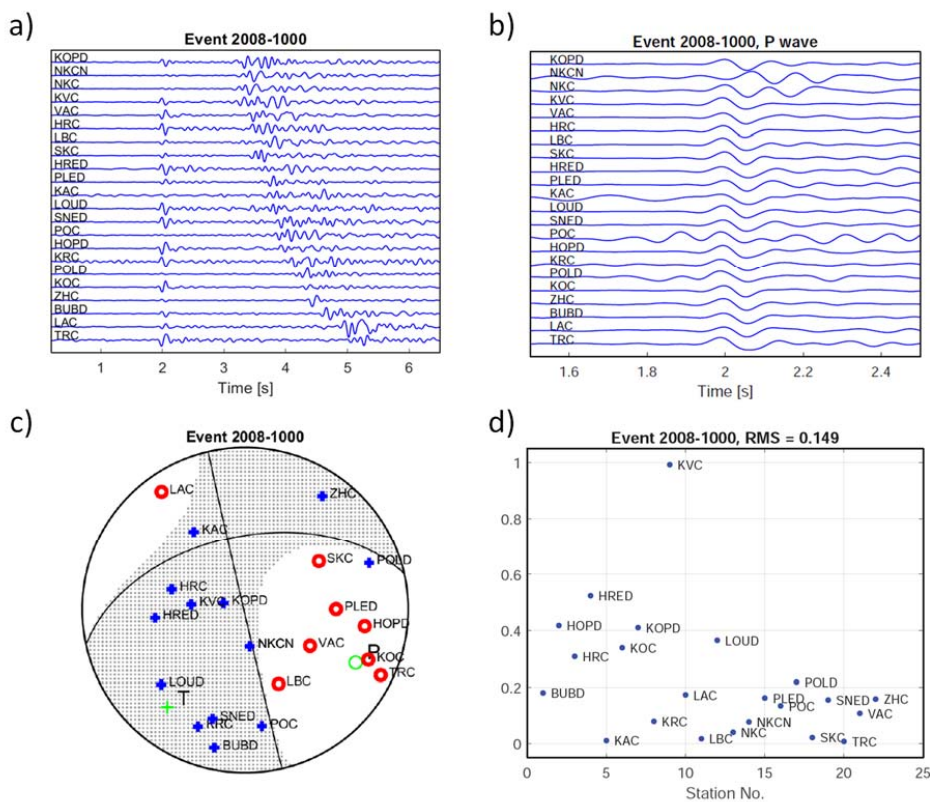
712

713

714



715
716
717
718
719
720
721
722
723
724
725
726
727



728
729
730
731
732
733
734
735
736
737
738
739
740
741
742
743
744

Figure 12. Example of plots provided for each earthquake in the dataset. (a) Vertical components of complete waveforms recorded at the WEBNET stations and aligned according to the arrival time of the P wave. Stations are sorted according to their epicentral distance. (b) Vertical components of the P waves aligned according to their arrival time and with a polarity switched according to the polarity of the common wavelet. (c) The focal mechanism with positions of the stations on the focal sphere (negative polarities – red circles, positive polarities – blue plus signs). (d) Root-mean-squares (RMS) of the differences between the theoretical and observed amplitudes of the P waves.

752
753

9 Discussion and conclusions

754
755
756
757
758
759

We publish a unique catalogue of moment tensors of microearthquakes that occurred in the West Bohemia in the period from 2008 to 2018. The catalogue is exceptional in several aspects: (1) it represents an extraordinary extensive dataset of more than 5.000 MTs, (2) it covers a long period of seismicity in the studied area, during which several prominent earthquake swarms took place, (3) the foci locations and retrieved MTs are of a very high accuracy. In addition, the three-component velocigrams recorded at the WEBNET stations together with



760 the velocity model in the region and the technical specification of stations are provided. This predetermines
761 the dataset to be utilized by a large community of researchers for various seismological purposes.

762

763 The great potential of the dataset or its subsets has so far been proved in studies of origins of the swarm activity
764 in this area (Horálek and Fischer, 2008; Fischer et al., 2010; Fischer et al., 2014), migration of seismicity in
765 time due to fluid flow and/or stress redistribution in the focal zone (Hainzl et al, 2012, 2016; Vavryčuk and
766 Hrubcová, 2017), changes of the v_p/v_s ratio in the focal zone (Dahm & Fischer, 2014; Bachura & Fischer,
767 2016), identification of fault segments and their mutual interaction (Vavryčuk and Adamová, 2018; Vavryčuk
768 et al., 2021), the fault instability (Vavryčuk, 2011b, 2014), differences in the seismic energy release in
769 earthquake swarms and mainshock-aftershock sequences (Čermáková and Horálek, 2015; Vavryčuk and
770 Adamová, 2018), the efficiency of new moment tensor inversion algorithms such as the MT inversion based
771 on the PCA (Vavryčuk et al., 2017), the MT inversion using the empirical Green's functions (Vavryčuk and
772 Adamová, 2020). The provided records were also utilized in a study of seismic anisotropy based on the analysis
773 of shear-wave splitting (Vavryčuk and Boušková 2008), identification of shallow discontinuities in the Earth's
774 crust (Hrubcová et al., 2016), lateral variation of depth of the Moho discontinuity (Hrubcová et al., 2013,
775 2017), and for detailed mapping of the non-DC components of MTs and shear-tensile fracturing in the Nový
776 Kostel focal zone (Vavryčuk, 20011a; Vavryčuk et al., 2021).

777

778 The dataset is ideal for being utilized in many other studies in future, e.g., for studies of (1) the interaction
779 between the scattered background regional seismicity and the swarm seismicity focused in the Nový Kostel
780 zone, (2) the Coulomb stress and local stress anomalies connected to fault irregularities, (3) diffusivity of fluids
781 along the activated faults, or (4) time-dependent seismic risk due to the migration of seismicity in the region.
782 In addition, the dataset is optimum for developing and testing new MT inversions (Šílený and Vavryčuk, 2000,
783 2002), stress inversions, and for the spatiotemporal evolution of tectonic stress. Since most of the earthquakes
784 are non-shear, the dataset can contribute to studies of the non-DC components and their relation to shear-tensile
785 fracturing and/or seismic anisotropy in the focal zone (Vavryčuk, 1997; Vavryčuk and Boušková, 2008).

786

787 **Data availability**

788 The waveforms are available at <https://doi.org/10.17632/4swk36hbvz.1> (Vavrycuk, 2021). For the review
789 purpose, the MT catalogue and other data are available at the following temporary link:
790 <https://drive.google.com/drive/folders/1HyFJO6aIwN5SctwsYp-GlhERspeVVz03?usp=sharing>. After the
791 acceptance of the paper, the temporary link will be substituted by a permanent doi number accessed under a
792 non-restrictive license CC BY.

793

794

795 **Acknowledgements**

796 The study was supported by the Grant Agency of the Czech Republic, Grant No. 19-06422S.

797



798 **References**

- 799 Bachura, M., and Fischer, T.: Detailed velocity ratio mapping during the aftershock sequence as a tool to
800 monitor the fluid activity within the fault plane, *Geophys. J. Int.*, 453, 215-222, 2016.
- 801 Bachura, M., Fischer, T., Doubravová, J., and Horálek, J.: From earthquake swarm to a main shock-
802 aftershocks: the 2018 activity in West Bohemia/Vogtland, *Geophys. J. Int.*, 224(3), 1835-1848, 2021.
- 803 Bankwitz, P., Schneider, G., Kämpf, H., and Bankwitz, E.: Structural characteristics of epicentral areas in
804 Central Europe: study case Cheb Basin (Czech Republic), *J. Geodyn.*, 35, 5-32.
805 [https://doi.org/10.1016/S0264-3707\(02\)00051-0](https://doi.org/10.1016/S0264-3707(02)00051-0), 2003.
- 806 Bath, M.: Lateral inhomogeneities in the upper mantle, *Tectonophysics*, 2, 483–514, 1965.
- 807 Bouchaala, F., Vavryčuk, V., and Fischer, T.: Accuracy of the master-event and double-difference locations:
808 Synthetic tests and application to seismicity in West Bohemia, Czech Republic, *J. Seismol.*, 17(3), 841-
809 859, <https://doi.org/10.1007/s10950-013-9357-4>, 2013.
- 810 Bräuer, K., Kämpf, H., Niedermann, S., and Strauch, G.: Monitoring of helium and carbon isotopes in the
811 western Eger Rift area (Czech Republic): Relationships with the 2014 seismic activity and indications for
812 recent (2000-2016) magmatic unrest, *Chem. Geol.*, 482, 131-145,
813 <https://doi.org/10.1016/j.chemgeo.2018.02.017>, 2018.
- 814 Čermáková, H., and Horálek, J.: The 2011 West Bohemia (Central Europe) earthquake swarm compared with
815 the previous swarms of 2000 and 2008, *J. Seismol.*, 19, 899–913. <https://doi.org/10.1007/s10950-015-9502-3>, 2015.
- 817 Červený, V.: *Seismic Ray Theory*. Cambridge University Press, Cambridge, 2001.
- 818 Cesca, S., and Dahm, T.: A frequency domain inversion code to retrieve time-dependent parameters of very
819 long period volcanic sources, *Comput. Geosci.*, 34(3), 235-246, 2008.
- 820 Cesca, S., Buforn, E., and Dahm, T.: Amplitude spectra moment tensor inversion of shallow earthquakes in
821 Spain, *Geophys. J. Int.*, 166, 839-854, 2006.
- 822 Dahm, T., and Fischer, T.: Velocity ratio variations in the source region of earthquake swarms in NW Bohemia
823 obtained from arrival time double- differences, *Geophys. J. Int.*, 196(2), 957-970, 2014.
- 824 Dreger, D., and Woods, B.: Regional distance seismic moment tensors of nuclear explosions, *Tectonophysics*
825 356, 139-156, 2002.
- 826 Fischer, T., Horálek, J., Michálek, J., and Boušková, A.: The 2008 West Bohemia earthquake swarm in the
827 light of the WEBNET network, *J. Seismol.*, 14, 665–682, 2010.
- 828 Fischer, T., Horálek, J., Hrubcová, P., Vavryčuk, V., Bräuer, K., and Kämpf, H.: Intra-continental earthquake
829 swarms in West-Bohemia and Vogtland: a review, *Tectonophysics*, 611, 1-27.
830 <https://doi.org/10.1016/j.tecto.2013.11.001>, 2014.
- 831 Fojtíková, L., Vavryčuk, V., Cipciar, A., and Madarás, J.: Focal mechanisms of micro-earthquakes in the Dobrá
832 Voda seismoactive area in the Malé Karpaty Mts. (Little Carpathians), Slovakia, *Tectonophysics*, 492,
833 213-229, <https://doi.org/10.1016/j.tecto.2010.06.007>, 2010.
- 834 Fojtíková, L., and Zahradník, J.: A new strategy for weak events in sparse networks: The first-motion polarity
835 solutions constrained by single-station waveform inversion, *Seismol. Res. Lett.*, 85(6), 1265-1274,
836 <https://doi.org/10.1785/0220140072>, 2014.
- 837 Ford, S.R., Dreger, D.S., and Walter, W.R.: Network sensitivity solutions for regional moment-tensor
838 inversions, *Bull. Seism. Soc. Am.*, 100(5A), 162-1970, 2010.
- 839 FeedMeImATroll: Suspension Bridge Picking Algorithm (SBPx)
840 ([https://www.mathworks.com/matlabcentral/fileexchange/51996-suspension-bridge-picking-algorithm-
841 sbpx](https://www.mathworks.com/matlabcentral/fileexchange/51996-suspension-bridge-picking-algorithm-sbpx)), MATLAB Central File Exchange, Retrieved September 21, 2021.
- 842 Frohlich, C.: Earthquakes with non-double-couple mechanisms, *Science*, 264(5160), 804-809, 1994.
- 843 Hainzl, S., Fischer, T., and Dahm, T.: Seismicity-based estimation of the driving fluid pressure in the case of
844 swarm activity in Western Bohemia, *Geophys. J. Int.*, 191(1), 271-278, 2012.



- 845 Hainzl, S., Fischer, T., Čermáková, H., Bachura, M., and Vlček, J.: Aftershocks triggered by fluid intrusion:
846 Evidence for the aftershock sequence occurred 2014 in West Bohemia/Vogtland, *J. Geophys. Res.*, 121(4),
847 2575–2590, 2016.
- 848 Horálek J., Fischer T., Boušková A., and Jedlička P.: The Western Bohemia/Vogtland region in the light of the
849 WEBNET network, *Stud. Geophys. Geod.*, 44(2), 107–125, 2000.
- 850 Horálek, J., and Fischer, T.: Role of crustal fluids in triggering the West Bohemia/Vogtland earthquake swarms:
851 just what we know (a review), *Stud. Geophys. Geod.*, 52, 455–478, 2008.
- 852 Hrubcová, P., Vavryčuk, V., Boušková, A., and Horálek, J.: Moho depth determination from waveforms of
853 microearthquakes in the West Bohemia/Vogtland swarm area, *J. Geophys. Res.*, 118, 1–17,
854 <http://dx.doi.org/10.1029/2012JB009360>, 2013.
- 855 Hrubcová, P., Vavryčuk, V., Boušková, A., and Bohnhoff, M.: Shallow crustal discontinuities inferred from
856 waveforms of microearthquakes: Method and application to KTB drill site and West Bohemia swarm area,
857 *J. Geophys. Res., Solid Earth*, 121, 881–902, <https://doi.org/10.1002/2015JB012548>, 2016.
- 858 Hrubcová, P., Geissler, W.H., Bräuer, K., Vavryčuk, V., Tomek, Č., and Kämpf, H.: Active magmatic
859 underplating in western Eger Rift, Central Europe, *Tectonics*, 36, <https://doi.org/10.1002/2017TC004710>,
860 2017.
- 861 Jakoubková, H., Horálek, J., and Fischer, T.: 2014 mainshock-aftershock activity versus earthquake swarms in
862 West Bohemia, Czech Republic, *Pure Appl. Geophys.*, 175(1), 109–131, [https://doi.org/10.1007/s00024-](https://doi.org/10.1007/s00024-017-1679-7)
863 [017-1679-7](https://doi.org/10.1007/s00024-017-1679-7), 2018.
- 864 Jechumtálová, Z., and Šílený, J.: Amplitude ratios for complete moment tensor retrieval, *Geophys. Res. Lett.*,
865 32, L22303, 2005.
- 866 Jost, M.L., and Hermann, R.B.: A student's guide to and review of moment tensors, *Seismol. Res. Lett.*, 60,
867 37–57, 1989.
- 868 Julian, B.R., Miller, A.D., and Foulger, G.R.: Non-double-couple earthquakes 1: Theory, *Rev. Geophys.*, 36,
869 525–549, 1998.
- 870 Kämpf, H., Bräuer, K., Schumann, J., Hahne, K., and Strauch, G.: CO₂ discharge in an active, non-volcanic
871 continental rift area (Czech Republic): Characterisation (delta C-13, He-3/He-4) and quantification of
872 diffuse and vent CO₂ emissions, *Chem. Geol.*, 339, 71–83,
873 <https://doi.org/10.1016/j.chemgeo.2012.08.005>, 2013.
- 874 Knopoff, L., and Randall, M.J.: The compensated linear vector dipole: A possible mechanism for deep
875 earthquakes, *J. Geophys. Res.*, 75, 4957–4963, 1970.
- 876 Kwiatek, G., Martínez-Garzón, P., and Bohnhoff, M.: HybridMT: A MATLAB/Shell environment package for
877 seismic moment tensor inversion and refinement, *Seismol. Res. Lett.*, 87(4), 964–976, 2016.
- 878 Lay, T., and Wallace, T.C.: *Modern Global Seismology*, Academic Press, New York, 1995.
- 879 Lomax, A., Michelini, A., and Curtis, A.: Earthquake location, direct, global-search methods, in *Complexity*
880 *In Encyclopedia of Complexity and System Science*, Part 5, Springer, New York, pp. 2449–2473,
881 <https://doi.org/10.1007/978-0-387-30440-3>, 2009.
- 882 Málek, J., Horálek, J., and Janský, J.: One-dimensional qP-wave velocity model of the upper crust for the West
883 Bohemia/Vogtland earthquake swarm region, *Stud. Geophys. Geod.*, 49, 501–524, 2005.
- 884 Miller, A.D., Foulger, G.R., and Julian, B.R.: Non-double-couple earthquakes 2: Observations, *Rev. Geophys.*,
885 36, 551–568, 1998.
- 886 Šílený, J.: Resolution of non-double-couple mechanisms: Simulation of hypocenter mislocation and velocity
887 structure mismodeling, *Bull. Seism. Soc. Am.*, 99(4), 2265–2272, 2009.
- 888 Šílený, J., and Milev, A.: Source mechanism of mining induced seismic events - Resolution of double couple
889 and non double couple models, *Tectonophysics*, 456(1–2), 3–15, 2008.
- 890 Šílený, J., and Vavryčuk, V.: Approximate retrieval of the point source in anisotropic media: numerical
891 modelling by indirect parametrization of the source, *Geophys. J. Int.*, 143, 700–708.
892 <https://doi.org/10.1046/j.1365-246X.2000.00256.x>, 2000.



- 893 Šílený, J., and Vavryčuk, V.: Can unbiased source be retrieved from anisotropic waveforms by using an
894 isotropic model of the medium? *Tectonophysics*, 356, 125-138, <https://doi.org/10.1016/S0040->
895 1951(02)00380-3, 2002.
- 896 Sokos, E., and Zahradník, J.: ISOLA — A Fortran code and Matlab GUI to perform multiple point source
897 inversion of seismic data, *Comput. Geosci.*, 34, 967–977, 2008.
- 898 Stierle, E., Vavryčuk, V., Šílený, J., and Bohnhoff, M.: Resolution of non-double-couple components in the
899 seismic moment tensor using regional networks: 1. A synthetic case study, *Geophys. J. Int.*, 196(3),
900 1869-1877, <https://doi.org/10.1093/gji/ggt502>, 2014.
- 901 Stierle, E., Bohnhoff, M., and Vavryčuk, V.: Resolution of non-double-couple components in the seismic
902 moment tensor using regional networks: 2. Application to aftershocks of the 1999 Mw 7.4 Izmit
903 earthquake, *Geophys. J. Int.*, 196(3), 1878-1888, <https://doi.org/10.1093/gji/ggt503>, 2014.
- 904 Vavryčuk, V.: Elastodynamic and elastostatic Green tensors for homogeneous weak transversely isotropic
905 media, *Geophys. J. Int.*, 130(3), 786-800. <https://doi.org/10.1111/j.1365-246X.1997.tb01873.x>, 1997.
- 906 Vavryčuk, V.: Spatially dependent seismic anisotropy in the Tonga subduction zone: a possible contributor to
907 the complexity of deep earthquakes, *Phys. Earth Planet. Inter.*, 155, 63-72.
908 <https://doi.org/10.1016/j.pepi.2005.10.005>, 2006.
- 909 Vavryčuk, V.: Tensile earthquakes: Theory, modeling, and inversion, *J. Geophys. Res., Solid Earth*, 116(B12),
910 B12320. <https://doi.org/10.1029/2011JB008770>, 2011a.
- 911 Vavryčuk, V.: Principal earthquakes: Theory and observations from the 2008 West Bohemia swarm, *Earth*
912 *Planet. Sci. Lett.*, 305, 290-296, <https://doi.org/10.1016/j.epsl.2011.03.002>, 2011b.
- 913 Vavryčuk, V.: Is the seismic moment tensor ambiguous at a material interface? *Geophys. J. Int.*, 194(1), 395-
914 400, <https://doi.org/10.1093/gji/ggt084>, 2013.
- 915 Vavryčuk, V.: Iterative joint inversion for stress and fault orientations from focal mechanisms, *Geophys. J. Int.*,
916 199(1), 69-77, <https://doi.org/10.1093/gji/ggu224>, 2014.
- 917 Vavryčuk, V.: Moment tensor decompositions revisited, *J. Seismol.*, 19(1), 231-252,
918 <https://doi.org/10.1007/s10950-014-9463-y>, 2015.
- 919 Vavryčuk, V.: WEBNET data 2008-2018, <https://doi.org/10.17632/4swk36hbvz.1>, 2021.
- 920 Vavryčuk, V., and Adamová, P.: Detection of stress anomaly produced by interaction of compressive fault steps
921 in the West Bohemia swarm region, Czech Republic, *Tectonics*, 37, 4212-4225.
922 <https://doi.org/10.1029/2018TC005163>, 2018.
- 923 Vavryčuk, V., Adamová, P., Doubravová, J., and Jakoubková, H.: Moment tensor inversion based on the
924 principal component analysis of waveforms: Method and application to microearthquakes in West
925 Bohemia, Czech Republic, *Seismol. Res. Lett.*, 88(5), 1303-1315, <https://doi.org/10.1785/0220170027>,
926 2017.
- 927 Vavryčuk, V., Adamová, P., Doubravová, J., and Ren, Y.: Mapping stress and fluids on faults by nonshear
928 earthquakes, *J. Geophys. Res.: Solid Earth*, 126, e2020JB021287, <https://doi.org/10.1029/2020JB021287>,
929 2021.
- 930 Vavryčuk, V., and Boušková, A.: S-wave splitting from records of local micro-earthquakes in West
931 Bohemia/Vogtland: An indicator of complex crustal anisotropy, *Stud. Geophys. Geod.*, 52, 631-650,
932 <https://doi.org/10.1007/s11200-008-0041-z>, 2008.
- 933 Vavryčuk, V., Bouchaala, F., and Fischer, T.: High-resolution fault image from accurate locations and focal
934 mechanisms of the 2008 swarm earthquakes in West Bohemia, Czech Republic, *Tectonophysics*, 590,
935 189-195, <https://doi.org/10.1016/j.tecto.2013.01.025>, 2013.
- 936 Vavryčuk, V., and Hrubcová, P.: Seismological evidence of fault weakening due to erosion by fluids from
937 observations of intraplate earthquake swarms, *J. Geophys. Res.*, 122,
938 <https://doi.org/10.1002/2017JB013958>, 2017.
- 939 Vavryčuk, V., and Kühn, D.: Moment tensor inversion of waveforms: a two-step time-frequency approach,
940 *Geophys. J. Int.*, 190, 1761-1776, <https://doi.org/10.1111/j.1365-246X.2012.05592.x>, 2012.



- 941 Waldhauser F. and Ellsworth W. L.: A double-difference earthquake location algorithm: Method and
942 application to the northern Hayward fault, California, *Bull. Seismol. Soc. Am.*, 90/6:1353–1368,
943 <https://doi.org/10.1785/0120000006>, 2000.
- 944 Yu, Ch., Vavryčuk, V., Adamová, P., and Bohnhoff, M.: Moment tensors of induced microearthquakes in The
945 Geysers geothermal reservoir from broadband seismic recordings: Implications for faulting regime, stress
946 tensor and fluid pressure, *J. Geophys. Res., Solid Earth*, 123, 8748-8766,
947 <https://doi.org/10.1029/2018JB016251>, 2018.
- 948 Yu, Ch., Vavryčuk, V., Adamová, P., and Bohnhoff, M.: Frequency-dependent moment tensors of induced
949 microearthquakes, *Geophys. Res. Lett.*, 46, 6406-6414, <https://doi.org/10.1029/2019GL082634>, 2019.
- 950 Zahradník, J., Sokos, E., Tselentis, G.-A., and Martakis, N.: Non-double-couple mechanism of moderate
951 earthquakes near Zakynthos, Greece, April 2006; explanation in terms of complexity, *Geophys. Prospect.*,
952 56, 341-356, 2008.
- 953
954